Research Square

Preprints are preliminary reports that have not undergone peer review.
They should not be considered conclusive, used to inform clinical practice,
or referenced by the media as validated information.

Broad-range controllable antisite defect engineering in gallium garnet crystals

Haohai Yu

haohaiyu@sdu.edu.cn

State Key Laboratory of Crystal Materials, Shandong University https://orcid.org/0000-0002-2295-1400

Zhaoshu Fu

State Key Laboratory of Crystal Materials, Shandong University

Yihao Shen

State Key Laboratory of Crystal Materials, Shandong University

Shuxian Wang

State Key Laboratory of Crystal Materials, Shandong University https://orcid.org/0000-0003-4995-7324

Dazhi Lu

State Key Laboratory of Crystal Materials, Shandong University https://orcid.org/0000-0002-7884-1286

Kui Wu

Shandong University

Ning Lu

Shandong University

Huaijin Zhang

Shandong University https://orcid.org/0000-0002-2118-5863

Article

Keywords:

Posted Date: October 26th, 2026

DOI: https://doi.org/10.21203/rs.3.rs-11427727/v1

License: This work is licensed under a Creative Commons Attribution 4.0 International License.
Read Full License

Additional Declarations: There is **NO** Competing Interest.

Abstract

Antisite defects are ubiquitous intrinsic cation-disorder imperfections in garnet crystals that exert pronounced impacts on a wide scope of functional properties critical to applications spanning optoelectronics, energy, and quantum technologies. However, rational broad-range control of antisite defects has remained a long-standing challenge, due to the limited fundamental mechanistic understanding of defect formation. Here, using $Lu_3Ga_5O_{12}$ (LuGG) — a gallium garnet archetype intrinsically prone to antisite formation — we confirm that the dominant antisite defects are Lu cations occupying octahedral Ga sites (denoted Lu_{Ga}), and develop a feasible, controllable antisite defect engineering strategy. By combining precursor homogenization to eliminate compositional fluctuations in the feed rods with crystal growth under pressurized O_2 to suppress Ga volatilization, we achieve an unprecedentedly wide tunable range of Lu_{Ga} antisite occupancy (1.6%–35%), far exceeding the modulation range reported for all previously studied gallium garnet systems. We further provide direct experimental evidence that antisite modulation enables systematic tailoring of the local crystal field environment of lanthanide Yb^{3+} activators, validating the critical role of antisite regulation in tuning the functional performance. This work establishes a general, programmable platform for rational defect-enabled design of garnet-based functional materials, which can be readily extended to other cation-disordered material systems for targeted performance optimization.

Introduction

Controllable defect engineering has emerged as a versatile strategy to tailor the functional performance of crystalline materials by modifying local coordination environments and associated material properties[1,2]. Garnets, which feature three distinct crystallographic cation sites (dodecahedral, octahedral, and tetrahedral)[3,4], represent a large family of functional materials with diverse applications spanning optoelectronics, energy, and quantum technologies, including solid-state lighting, lasers[4,5], scintillation detection, magneto-optical devices[6,7], and solid-state lithium batteries[8]. The characteristic multi-site crystallographic architecture of garnets inherently predisposes this material family to antisite defect formation[3,9], where cations exchange their native lattice positions, disrupting global cation ordering and triggering local structural rearrangements. Accordingly, fundamental mechanistic understanding and precise control of antisite defects in garnets offer a straightforward, robust pathway to establishing unambiguous structure-defect-property correlations linking defect configurations, local atomic arrangements, and macroscopic functional responses[2,10,11].

Manipulating antisite defects in garnet crystals has long been a central research focus: probing the effects of perturbed local coordination environments enables unambiguous elucidation of intrinsic material properties[3,9,12,13]. Across application domains, antisite regulation delivers predictable performance modulation: for luminescent, scintillation, and laser garnets, it tailors the spectral characteristics and cross-relaxation pathways of activator dopants[2,11], redirects carrier recombination pathways, modulates decay dynamics[6,14], and expands the structural design space for spectroscopic

optimization; for magnetic garnets, antisite-mediated cation redistribution alters sublattice magnetization and superexchange interactions[10,15], offering a robust structural handle for engineering high-performance magneto-optical devices; for garnet-type solid electrolytes, antisite-induced cation-site disorder modulates Li^+ migration kinetics[16,17], opening an alternative structural design avenue for high-conductivity solid electrolytes. Nevertheless, despite extensive research progress[2,11], controllable antisite defect regulation in garnets remains a long-standing unresolved challenge, particularly for host lattices where the radii of cations occupying distinct crystallographic sites are closely matched. This persistent knowledge gap has severely hindered both mechanistic elucidation of antisite formation and full exploitation of defect-mediated performance optimization, creating an urgent demand for generalizable, actionable strategies for controllable antisite defect engineering in garnets.

To address this critical open challenge, this work selects $Lu_3Ga_5O_{12}$ (LuGG), a prototypical gallium garnet with an intrinsically high propensity for antisite defect formation owing to the close ionic radii of Lu^{3+} and Ga^{3+}, as our model research system[5,18]. Conventional LuGG crystal growth suffers from irreproducible antisite concentrations caused by uncontrolled volatilization of gallium-containing precursors. Guided by the Lu_2O_3-Ga_2O_3 binary phase diagram, we reveal the origin of antisite defect formation in the LuGG host and develop a generalizable protocol for tuning antisite defect concentrations. Systematic structural characterization confirms that the dominant antisite defect species in LuGG is the Lu_{Ga} antisite, where Lu^{3+} cations occupy the nominal octahedral Ga^{3+} sites. By combining precursor composition homogenization and optical floating zone (OFZ) crystal growth under pressurized O_2, we achieve broad-range tuning of Lu_{Ga} antisite concentration over one order of magnitude, spanning from 35% down to 1.6%. We further demonstrate that varying Lu_{Ga} antisite concentrations induces pronounced modulation of the crystal-field splitting environment for doped Yb^{3+} activators via local coordination structure modification, explicitly validating the effectiveness of our regulation strategy. These findings establish a mechanism-guided paradigm for controllable antisite defect engineering in garnets, providing a robust foundation for future exploration of defect-mediated property modulation and development of high-performance garnet-based functional devices.

Antisite-defect regulation strategy

Garnet-type oxides adopt the general stoichiometry $A_3B_2C_3O_{12}$, in which large rare-earth (RE) cations predominantly occupy eight-coordinate dodecahedral A sites, while smaller trivalent cations (e.g., Ga^{3+}, Fe^{3+}, and Al^{3+}) partition between six-coordinate octahedral B sites and four-coordinate tetrahedral C sites[19]. Despite the strong site preference dictated by ionic radius and coordination geometry, cation antisite disorder between A and B sites is a pervasive structural feature in garnet lattices. The resulting local coordination distortions and perturbed crystal-field environments dramatically tune the physicochemical properties of garnets, including scintillation response[20], lasing efficiency[5], and magneto-optical activity[21]. Accordingly, rational manipulation of antisite defect populations is a critical prerequisite for unlocking the full performance potential of functional garnet crystals for practical

applications. Among lanthanide RE cations that typically occupy A sites, Lu^{3+} has an ionic radius closest to that of conventional B-site cations, endowing it with an inherently high propensity for antisite occupation at the B site. Herein, we select LuGG as a model system to investigate antisite defect control: owing to its pronounced intrinsic tendency toward antisite formation, LuGG serves as an ideal platform for dissecting the fundamentals of antisite formation and its regulation. In LuGG, Lu^{3+} nominally occupies dodecahedral A sites, while Ga^{3+} partitions between octahedral B and tetrahedral C sites. Two typical antisite defect configurations can form: Lu_{Ga} and Ga_{Lu}[22], corresponding to Lu^{3+} at octahedral sites and Ga^{3+} at dodecahedral sites, respectively. Prior theoretical calculations have confirmed that Lu_{Ga} antisite defects exhibit substantially lower formation energies than Ga_{Lu} defects, a trend that is consistent with the experimentally observed lattice expansion in gallium garnets that accompanies increasing antisite defect content[3,23].

To achieve rational antisite control, resolving the microscopic accommodation mechanism underlying antisite formation and developing strategies to tailor site occupation preference during crystal growth are both critical core requirements for the field. For the prevalent Lu_{Ga} antisites widely observed in LuGG, excess Lu^{3+} ions are spontaneously incorporated into octahedral B sites, indicating that the garnet crystal structure is preferentially stabilized for compositions slightly off-stoichiometry on the Lu-rich side, relative to the nominal Lu:Ga stoichiometry (3:5)[24]. This broad single-phase stability window on the Lu-rich side contrasts sharply with the narrow single-phase region observed for aluminum-based garnets, further highlighting that precise phase-composition control is indispensable during the bulk crystal growth of LuGG. For the conventional Czochralski growth of gallium garnet bulk crystals, the commonly applied inert atmosphere protection severely exacerbates the volatilization of gallium-based precursors from the melt. This gradually shifts the melt composition away from the nominal stoichiometry toward a Lu-rich state, in turn progressively promoting the formation of Lu_{Ga} antisite defects[23,24]. As a result, maintaining a stable LuGG melt composition throughout long-duration growth runs remains extremely challenging, and the production of high-quality as-grown LuGG crystals with precisely tunable antisite concentrations remains challenging.

OFZ crystal growth offers a versatile platform for the bulk preparation of gallium-based garnet crystals, owing to its unique crucible-free configuration that relies on a surface-tension-stabilized floating melt zone[25,26]. This feature eliminates crucible-induced atmospheric limitations and enables robust control of both melt composition and gallium source volatilization, providing a promising alternative pathway for tuning antisite defect content in LuGG. To address the long-standing challenge of controllable antisite defect formation in LuGG, we develop a rationally optimized OFZ growth strategy based on the synergistic tuning of two core growth parameters: feed rod precursor quality and growth atmosphere. For feed rod optimization, we demonstrate that switching raw oxide precursors from conventional micron-sized starting powders to nano-sized powders, combined with homogeneous mixing via ball milling, markedly improves the bulk compositional homogeneity of the consolidated feed rod. This eliminates the heterogeneous composition distribution inherent to traditional micron-powder-derived

feed rods, effectively stabilizing floating melt zone composition during growth and greatly facilitating precise control of antisite defect populations. Furthermore, we implement OFZ growth under a pressurized O_2 atmosphere of 4 bar to further suppress the volatilization of the Ga source, yielding additional improvements in the compositional homogeneity of as-grown crystals. Systematic experimental validation confirms that our strategy achieves broad tunability of Lu_{Ga} antisite defect concentrations over an exceptionally wide range, from 35% down to 1.6%. This synergistic growth strategy provides a transferable blueprint for understanding and controlling non-stoichiometry-driven antisite defects in a broad family of gallium garnet systems.

Micron-scale compositional homogenization

We began with a systematic investigation of the effect of Ga_2O_3 compensation on the modulation of Lu_{Ga} antisite defects, using wet-mixed micron-sized precursors. Given that volatilization of Ga sources during high-temperature crystal growth causes deviations from nominal Lu/Ga stoichiometry, we designed a series of precursors with intentional Ga excess to probe the effect of stoichiometric tuning on antisite defect populations, fixing the growth rate at a constant 6 mm h^{-1} at ambient pressure across all samples to exclude growth-rate-induced variations. As summarized in Supplementary Fig. 1, the characteristic diffraction peak of the uncompensated sample exhibits a 0.14° low-angle shift relative to the stoichiometric LuGG standard reference (ICDD PDF card No. 73-1372).

To further characterize antisite defects in as-grown LuGG crystals, we mapped cation distributions at the atomic scale by combining high-angle annular dark-field scanning transmission electron microscopy (HAADF-STEM) and energy-dispersive X-ray spectroscopy (EDS) mapping[10,27]. The choice of observation orientation is critical to resolving cations located at different polyhedral crystallographic sites. Along the < 100 > and < 110 > projections, overlap between dodecahedral and tetrahedral sites makes unambiguous identification of cation occupancies challenging. By contrast, the < 111 > projection enables clear resolution of all three distinct cation sites, making it ideal for direct screening of antisite defects (Supplementary Fig. 2). To enable fabrication of a well-oriented lamella, we first used electron backscatter diffraction (EBSD) to index the < 111 > crystallographic orientation of the bulk crystal, then fabricated the target lamella via focused ion beam (FIB) milling. As exhibited in Fig. 2a, the HAADF-STEM image reveals a well-ordered periodic arrangement of atomic columns, matching the projected Lu and Ga atomic distribution expected for the LuGG structure along < 111>, indicating that the imaging conditions were suitable for atomic-scale structural analysis. EDS mapping further reveals Lu signals at nominally octahedral Ga sites. This observation directly confirms the presence of Lu_{Ga} antisite defects at these positions along the imaging orientation, in agreement with prior findings, and yields a refined lattice parameter of 12.247 Å, corresponding to a Lu_{Ga} antisite defect population of 20%.

As shown in Supplementary Fig. 1, at a moderate Ga_2O_3 compensation level of 3 wt.%, the Lu_{Ga} antisite population is reduced to 15%, accompanied by a corresponding lattice contraction to 12.215 Å—a trend

fully consistent with the smaller ionic radius of octahedrally coordinated Ga^{3+} relative to Lu^{3+}[18]. However, when the Ga_2O_3 compensation level is further increased to 5 wt.%, the refined lattice parameter (12.214 Å) remains nearly identical to that of the 3 wt.% sample, indicating that excess Ga can no longer be incorporated into the garnet lattice. Instead, excess Ga segregates out of the bulk garnet lattice to form precipitates of the β-Ga_2O_3 secondary phase, as confirmed by structural characterization (Supplementary Fig. 1). These results collectively demonstrate that single-parameter Ga compensation alone can only tune Lu_{Ga} antisite populations over a limited range, reducing defect content from 20% to 15%. Excess Ga_2O_3 does not further improve the crystalline quality of the as-grown crystals, and instead only precipitates as an unwanted secondary phase.

Subsequently, we performed systematic growth optimization using identical wet-mixed micron-sized precursors with a standard Lu:Ga stoichiometry (3:5). We varied the residence time of the feed rod in the high-temperature molten zone to investigate the additional structural deviation introduced during single-crystal growth[28]. As illustrated in Fig. 2b–d, LuGG single crystals were successfully obtained across growth rates ranging from 6 mm h^{-1} to 30 mm h^{-1}. With increasing growth rate, the characteristic {420} diffraction peak shifts progressively toward the standard reference position for growth rates between 6 mm h^{-1} and 20 mm h^{-1}; after this range, the peak position evolves gradually for growth rates from 20 mm h^{-1} to 30 mm h^{-1} (Supplementary Fig. 3). Increasing the growth rate reduces the Rietveld-refined lattice parameter from 12.247 Å (at 6 mm h^{-1}) to 12.206 Å (at 30 mm h^{-1}), which corresponds to a reduction in Lu_{Ga} antisite defect population from 20% to 9%.

To further corroborate the influence of growth rate on antisite defect formation, we quantified the normalized mass loss, defined as the total mass loss during crystal growth normalized by the mass of the as-grown crystal. As shown in Supplementary Fig. 4 and Supplementary Table 1, the trend between normalized mass loss and growth rate matches well the evolution of the refined structural parameters. These findings confirm that growth rate is a robust strategy to tune the Lu_{Ga} antisite defect population: varying growth rate adjusts the residence time of the feed rod in the molten zone, which in turn controls the cumulative volatilization loss of the Ga-based source[29,30]. Interestingly, the characteristic {420} diffraction peak of LuGG crystals grown at 30 mm h^{-1} closely matches that of the starting wet-mixed micron-sized feed rod (Supplementary Fig. 5). These observations indicate that the compositional uniformity of the feed rod strongly impacts the accessible range of Lu_{Ga} antisite defect concentrations, and thus sets the upper limit of this defect optimization approach. Accordingly, further precise tuning of Lu_{Ga} antisite defects requires simultaneous direct control over both the structural baseline predetermined by the precursor and the growth-induced loss of Ga-containing species.

Coupled nanoscale homogenization and pressurized O crystal growth

To address the limited tunability of Lu_{Ga} antisite defects associated with wet-mixed micron-sized (*μ*-WM) feed rods of standard Lu:Ga stoichiometry (3:5), we implemented ball milling to further improve the compositional homogeneity of precursor raw materials[31,32]. We prepared two types of ball-milled precursors for feed rod fabrication: ball-milled micron-sized powders (*μ*-BM) and ball-milled nanopowders (*n*-BM). Scanning electron microscopy (SEM) coupled with line-scan energy-dispersive spectroscopy (EDS) mapping reveals that the Lu/Ga atomic ratio in the sintered *μ*-WM feed rod has a root-mean-square deviation (RMSD) of 24.3% relative to the target stoichiometric value of 0.60. The RMSD drops to 8.1% for *μ*-BM feed rods, and reaches a minimum of 4.2% for *n*-BM feed rods. These quantitative results confirm that nanoscale mixing markedly suppresses local Lu/Ga compositional fluctuations within sintered feed rods. As shown in Fig. 3b and Supplementary Fig. 6, XRD characterization demonstrates that the characteristic {420} diffraction peaks of *μ*-BM and *n*-BM feed rods align far more closely with the standard LuGG reference pattern than those of *μ*-WM feed rods. The magnitude of the peak low-angle shift decreases from ~ 0.05° for *μ*-WM, to ~ 0.02° for *μ*-BM, and to nearly 0° for *n*-BM. This trend verifies that improved compositional homogeneity effectively brings the bulk stoichiometry of the feed rod into close agreement with the target standard 3:5 Lu:Ga ratio.

We next grew and compared LuGG single crystals from all three types of feed rods under identical growth conditions: a constant growth rate of 15 mm h^{-1} at ambient pressure. As shown in Fig. 3c, Rietveld refinement of XRD data yields refined lattice parameters of 12.220 Å (*μ*-WM), 12.207 Å (*μ*-BM), and 12.198 Å (*n*-BM), corresponding to Lu_{Ga} antisite defect populations of 11%, 9%, and 6.8%, respectively. These results confirm that improving the compositional homogeneity of the precursor feed rod effectively suppresses Lu_{Ga} antisite defect formation in as-grown crystals by eliminating precursor-induced compositional fluctuations. Nevertheless, unavoidable volatilization of Ga-containing species during crystal growth means the stoichiometry of the final as-grown *n*-BM crystal still does not match that of the starting sintered feed rod[23,29], and a residual low-angle shift of ~ 0.02° remains relative to the standard {420} diffraction peak of stoichiometric LuGG (Fig. 3d and Supplementary Fig. 7).

To mitigate evaporation during OFZ crystal growth, employing a pressurized growth atmosphere is a well-established effective strategy, which has already proven successful for the fabrication of a wide range of optoelectronic functional crystals[33,34]. To further expand the tunability range of Lu_{Ga} antisite defects, we grew LuGG crystals using the *n*-BM feed rod under a pressurized O_2 atmosphere of 4 bar at a growth rate of 15 mm h^{-1}. As illustrated in Fig. 4a, the severe volatilization observed under ambient pressure for both *μ*-WM and *n*-BM growth is effectively suppressed under pressurized conditions. Specifically, the normalized mass loss decreased from 5.7% for *μ*-WM-6 and 2.6% for *n*-BM-15 to merely 0.88% for HP-*n*-BM-15 (Fig. 4b). The {420} diffraction peak of the HP-*n*-BM-15 crystal aligns nearly perfectly with the corresponding peak of the *n*-BM feed rod and the stoichiometric LuGG (Fig. 4c), confirming that Ga volatilization has been effectively mitigated. Rietveld refinement further yielded a lattice parameter of 12.189 Å for this crystal grown under pressurized O_2, which closely approaches the reference value of 12.188 Å for stoichiometric LuGG, corresponding to a Lu_{Ga} antisite defect concentration of 1.6% (Supplementary Fig. 8 and Supplementary Table 2). As shown in Fig. 4d, the

HAADF-STEM image of the crystal grown under a pressurized O_2 atmosphere confirms excellent atomic ordering along the < 111 > viewing direction. EDS elemental mapping of Lu further confirms that the concentration of Lu_{Ga} antisite defects in HP-*n*-BM-15 is substantially reduced relative to that in the aforementioned *μ*-WM-6 sample, in excellent agreement with our prior structural refinement results (Fig. 4e). Collectively, these results demonstrate that, when combined with compositionally uniform feed rods, OFZ growth under pressurized O_2 can effectively reduce the formation of Lu_{Ga} antisite defects by suppressing Ga volatilization throughout the entire growth process.

To further elucidate the influence of antisite defects on the local crystalline lattice, we quantified differences in atomic arrangement between the *μ*-WM-6 and HP-*n*-BM-15 specimens. Motivated by the formation origin of Lu_{Ga} antisite defects, we measured the projected distances between Ga1 atomic columns and their nearest-neighbor Lu atomic columns (denoted d_{Ga1-Lu}). Six projected d_{Ga1-Lu} values were extracted for each Ga1 column for statistical analysis (Fig. 4f), with the corresponding local-distance mapping of the high-antisite *μ*-WM-6 crystal provided in Supplementary Fig. 9. As shown in Fig. 4g,h, the *μ*-WM-6 specimen exhibits a far more dispersed d_{Ga1-Lu} distribution relative to HP-*n*-BM-15, giving a standard deviation (σ) of 0.052 Å — approximately 1.44 times that of the HP-*n*-BM-15 specimen (0.036 Å). In an ideal defect-free lattice, all projected Ga1–Lu nearest-neighbor distances along the < 111 > viewing direction would be identical. This pronounced discrepancy in d_{Ga1-Lu} distribution between the two LuGG samples confirms that the formation of Lu_{Ga} antisite defects not only induces macroscopic lattice expansion, but also introduces distinct local structural perturbations at the atomic scale. This result verifies that tailoring antisite defect concentrations in garnet crystals enables targeted local structural modification, creating a robust platform to establish a direct correlation between antisite defect regulation and local property responses.

Antisite-defect-induced local crystal-field variation of Yb

Given the broad tunability of Lu_{Ga} antisite defect concentrations achieved in this study, we employed trivalent lanthanide RE^{3+} luminescent ions to further elucidate the underlying influence mechanism. Yb^{3+} was selected as the probe ion owing to its high sensitivity to changes in the local coordination environment, as well as its important applications in the 1-*μ*m lasing field[35,36], including ultra-strong and ultrafast laser systems. As shown in Fig. 5a, the $4f^{13}$ configuration of Yb^{3+} comprises only two manifolds: the $^2F_{7/2}$ ground state and $^2F_{5/2}$ excited state, which split into four and three Kramers doublets, respectively[37,38]. This well-defined Stark-level structure produces well-resolved transition lines between distinct energy levels. Notably, the zero-phonon line (ZPL) transition between the lowest crystal-field splitting levels of the $^2F_{7/2}$ and $^2F_{5/2}$ manifolds can directly reflect changes in local coordination environments[39]. Accordingly, 0.5 at.% Yb^{3+} was incorporated into the LuGG lattice, and the corresponding emission spectra were collected at 78 K to reduce phonon-induced spectral interference. Four distinct Yb:LuGG samples were prepared: *μ*-WM-6, *μ*-BM-15, *n*-BM-15, and HP-*n*-BM-15, with

corresponding Lu_{Ga} antisite defect concentrations of 20%, 9%, 6.8%, and 1.6%, respectively. As demonstrated in Fig. 5b, all samples exhibit the characteristic Yb^{3+} emission, with a primary emission peak centered at ~ 1024 nm[40]. The most prominent difference between samples occurs in the ZPL region: three distinct Yb^{3+} luminescent centers are resolved, in contrast to the theoretically predicted single transition peak for a homogeneous garnet lattice. The four samples show clear differences in ZPL spectral features, demonstrating that variations in antisite defect concentration strongly modify the relative spectral contributions of different Yb^{3+} centers. To quantitatively evaluate these discrepancies, we assigned the three emission peaks centered at 10323 cm^{-1}, 10327 cm^{-1}, and 10331 cm^{-1} to Yb_{I}, Yb_{II}, and Yb_{III}, respectively, and performed Gaussian fitting to resolve the relative contribution of each component. As shown in Fig. 5c, with the Lu_{Ga} antisite occupancy decreased from 20% to 1.6%, the normalized integrated areas of Yb_{I} and Yb_{III} decrease from 67.57% to 26.23% and from 26.46% to 11.42%, respectively, while the normalized area of Yb_{II} increases from 5.98% to 62.35%.

Next, we systematically analyzed the influence of antisite defects on the local coordination configurations of Yb^{3+} (Fig. 5d). As demonstrated above, a reduction in Lu_{Ga} antisite defect concentration leads to a decrease in the relative population of Yb_{I} and Yb_{III} centers and a corresponding increase in the population of Yb_{II}. This indicates that the local coordination environments of Yb_{I} and Yb_{III} are strongly correlated with Lu_{Ga} antisite defects, while Yb_{II} centers are located away from antisite positions. Furthermore, according to previous crystal-field splitting studies of Yb^{3+}-doped optical materials, low coordination numbers and short ligand bond lengths of Yb^{3+} favor the formation of high-energy ZPL transition lines[45]. For example, in Yb:$Ca_3(Nb,Ga)_5O_{12}$ garnet, the ZPL lines of octahedral and dodecahedral Yb^{3+} centers are located at ~ 10323 cm^{-1} and ~ 10288 cm^{-1}, respectively[46]; and in orthorhombic Yb:$LaLuO_3$ sesquioxide, the ZPL lines of octahedral and dodecahedral Yb^{3+} centers are positioned at ~ 10288 cm^{-1} and ~ 10178 cm^{-1}, respectively[47,48]. Following this established trend, the Yb_{III} center in Yb:LuGG is assigned to Yb^{3+} occupying octahedral sites, while Yb_{II} corresponds to Yb^{3+} located at dodecahedral sites. In contrast, the emergence of the Yb_{I} center is closely associated with the formation of Lu_{Ga} antisite defects. Its ZPL energy is very close to that of Yb_{II}, indicating that Yb_{I} also tends to occupy dodecahedral sites, and the transition energy deviation between Yb_{I} and Yb_{II} originates from the altered neighboring cationic coordination environment. When Lu_{Ga} antisite defects are suppressed in the HP-*n*-BM-15 sample, Yb_{II} becomes the dominant luminescent center, confirming that its coordination environment is nearly identical to that of the ideal garnet dodecahedral site, which is surrounded by four GaO_6 octahedra. For Yb_{I}, by contrast, adjacent GaO_6 octahedra are partially replaced by LuO_6 octahedra due to the presence of Lu_{Ga} antisite defects, giving rise to the significant ZPL energy difference between the two dodecahedral Yb^{3+} centers. This phenomenon further highlights the importance of antisite defect control in manipulating the crystal-field splitting of Yb^{3+}, particularly for understanding the intrinsic transition properties of Yb^{3+} sites in garnet lattices[40,49,50].

Discussion

Antisite defects in garnet crystals have remained a long-standing topic of research over the past decades, owing to their pronounced influence on physicochemical properties[51,52]. Rational control over antisite defect formation is therefore of critical importance for optimizing the performance of garnet-based materials in practical applications. However, the high-temperature complex growth environment, combined with an incomplete understanding of the underlying control mechanisms, renders antisite defect engineering particularly challenging[53]; consequently, most studies have been confined to theoretical analyses. Inspired by the phase diagram distribution, we herein propose a feasible and controllable strategy for antisite defect management in LuGG garnet crystals, which inherently exhibit prevalent Lu_{Ga} antisite defects. By mitigating precursor-induced compositional fluctuations in the feed rods and suppressing Ga volatilization during crystal growth, we successfully achieved a remarkably wide, accessible control window for Lu_{Ga} antisite defects, spanning 1.6% to 20%. On that basis, by employing a *μ*-WM Lu-rich feed with a nominal Lu:Ga ratio of 3.5:4.5, we further obtained a single-phase garnet crystal with approximately 35% Lu_{Ga} antisite occupancy (Supplementary Fig. 10 and Supplementary Table 2), which ultimately extends the overall tunable occupancy range achieved in this work to 1.6%–35%. Benchmarking this accessible range against previously reported antisite modulation ranges in gallium garnets (Fig. 5e) further highlights the extent of defect regulation realized in LuGG, despite its intrinsically high antisite formation propensity[23,24,41–44]. More importantly, subsequent ZPL spectral analysis of Yb^{3+} provides direct experimental evidence that antisite defect regulation effectively tailors the local crystal-field splitting through controlled modifications of the coordination environment correlated with antisite defects. This finding underscores the fundamental importance of antisite control in guiding the design and targeted tuning of the spectroscopic performance of lanthanide-activated ions in garnet hosts[54].

Antisite defects are ubiquitous intrinsic imperfections in garnet crystals, arising from the cation exchange between inequivalent crystallographic sites during high-temperature crystal growth or post-growth annealing. These defects play a critical role in dictating a diverse array of functional properties across numerous practical applications, including solid-state lighting, high-efficiency lasers, fast scintillation detection[55], magneto-optical modulation[56], and lithium-ion solid-state electrolytes[57]. Far from being mere structural imperfections, antisite defects act as local perturbators of the crystal field and material properties, offering a powerful handle for property engineering. Accordingly, the antisite defect regulation strategy developed here provides a feasible and systematic route for the programmable design of custom defect architectures—enabling not just passive accommodation but active engineering of defect populations with atomic-scale precision. This approach creates a significantly broader design space for optimizing the targeted functional performance of garnet-based materials, shifting the paradigm from empirical screening to rational defect-enabled design. This strategy holds profound significance not only for display technologies, radiation detection, and laser systems—all of which are fundamentally governed by energy-level transition processes—but also for emerging frontiers such as spintronics[58], where defect-induced magnetic moments can be harnessed[59],

and next-generation all-solid-state lithium-ion batteries[60], where ion transport efficiency is paramount. Moreover, the paradigm developed here can be readily extended to other optoelectronic material systems, including perovskites, spinels, and sesquioxides, where analogous cation-site disorder often dictates performance. It offers an alternative optimization route to rationally manipulate structural defects to meet corresponding application demands, particularly for systematically exploring the intricate interplay between a material's crystal structure and its target performance.

Conclusion

In this work, we unambiguously identify the dominant antisite defects in LuGG garnet as Lu cations occupying octahedral Ga sites (Lu_{Ga}) via combined structural characterization, including structural refinement and local atomic-scale microstructural analysis. Building on this structural insight, we develop a mechanism-guided strategy for broad-range antisite engineering in LuGG via synergistic control of precursor compositional homogeneity and Ga volatilization during crystal growth. This strategy delivers an unprecedentedly wide tunable range of Lu_{Ga} antisite occupancy (1.6%–35%), far broader than the modulation ranges reported for all other gallium garnet systems. We further demonstrate that tuning Lu_{Ga} antisite concentration systematically modulates the ZPL spectral profile and crystal-field splitting of doped Yb^{3+} ions, driven by antisite-induced local coordination environment variation. These findings establish antisite regulation as an experimentally feasible route for exploring structure–defect–property relationships and tailoring the functional performance of garnet-based materials, advancing fundamental understanding of the correlation between atomic-scale structural defects and target material performance.

Declarations

Data availability

The experimental data generated in this study are provided in the Supplementary Information/Source data file. The uploaded source data include the data obtained that can reproduce all the findings of this study. Source data are provided with this paper.

Acknowledgments

This work is supported by the National Natural Science Foundation of China (grant nos. 52472008 (S.W.), 52622202 (S.W.), 52025021 (H.Y.), U24A2027 (S.W.)), the Taishan Scholar Young Experts Program of Shandong Province (Grant No. tsqn202507055 (K.W.)), and the Future Plans of Young Scholars at Shandong University (S.W.).

Author contributions

S.W., H.Y. and H.Z. conceived and supervised the research. Z.F. designed and carried out the crystal growth and antisite-defect regulation experiments, performed the structural and spectroscopic

characterizations, and analyzed the experimental data. Y.S. assisted with crystal growth, sample preparation, and related characterizations. N.L. performed the electron microscopy characterization and contributed to the local structural and bond-length analyses. D.L. and K.W. contributed to scientific discussions and interpretation of the experimental results. Z.F. and S.W. wrote the original manuscript. S.W., N.L., H.Y. and H.Z. reviewed and revised the manuscript. All authors discussed the results and approved the final manuscript.

Competing interests

The authors declare no competing interests.

References

1. Tsai JY, Pan J, Lin H, Bansil A, Yan Q (2022) Antisite defect qubits in monolayer transition metal dichalcogenides. Nat Commun 13:492
2. Cao W et al (2023) Highly nonstoichiometric YAG ceramics with modified luminescence properties. Adv Funct Mater 33:2213418
3. Milanese C, Buscaglia V, Maglia F, Anselmi-Tamburini U (2004) Disorder and nonstoichiometry in synthetic garnets $A_3B_5O_{12}$ (A = Y, Lu–La, B = Al, Fe, Ga): a simulation study. Chem Mater 16:1232–1239
4. Xia Z, Meijerink A (2017) Ce^{3+}-doped garnet phosphors: composition modification, luminescence properties and applications. Chem Soc Rev 46:275–299
5. Wu K et al (2012) $Lu_3Ga_5O_{12}$ crystal: exploration of new laser host material for the ytterbium ion. J Opt Soc Am B 29:2320–2328
6. Zhu D, Nikl M, Chewpraditkul W, Li J (2022) Development and prospects of garnet ceramic scintillators: a review. J Adv Ceram 11:1825–1848
7. Zhang L et al (2023) A review on magneto-optical ceramics for Faraday isolators. J Adv Ceram 12:873–915
8. Kim S et al (2022) High-energy and durable lithium metal batteries using garnet-type solid electrolytes with tailored lithium-metal compatibility. Nat Commun 13:1883
9. Muñoz-García AB, Artacho E, Seijo L (2009) Atomistic and electronic structure of antisite defects in yttrium aluminum garnet: density-functional study. Phys Rev B 80:014105
10. Rosenberg E et al (2023) Revealing site occupancy in a complex oxide: terbium iron garnet. Small 19:2300824
11. Fang X et al (2026) Persistent luminescence in highly nonstoichiometric GAGG garnets $Gd_{3+x}[Al_2Ga_3]_{1-x/5}O_{12}$ ($0 \le x \le 0.6$) doped with Ce^{3+}/Cr^{3+}. Adv Opt Mater 14:e02509
12. Kwapisz R, Cone RL, Thiel CW (2022) Quantifying antisite defect concentrations in yttrium aluminum garnet by high-precision density analysis. J Lumin 252:119408

13. Fang X et al (2024) Realization of extreme nonstoichiometry in gadolinium aluminate garnets by glass crystallization synthesis. Chem Mater 36:8555–8563
14. Fasoli M et al (2011) Band-gap engineering for removing shallow traps in rare-earth $Lu_3Al_5O_{12}$ garnet scintillators using Ga^{3+} doping. Phys Rev B 84:081102
15. Santiso J et al (2023) Antisite defects and chemical expansion in low-damping, high-magnetization yttrium iron garnet films. ChemNanoMat 9:e202200495
16. Anderson E, Zolfaghar E, Jonderian A, Khaliullin RZ, McCalla E (2024) Comprehensive dopant screening in $Li_7La_3Zr_2O_{12}$ garnet solid electrolyte. Adv Energy Mater 14:2304025
17. Yan Z, Zhu Y (2024) Impact of lithium nonstoichiometry on ionic diffusion in tetragonal garnet-type $Li_7La_3Zr_2O_{12}$. Chem Mater 36:11551–11557
18. Shannon RD (1976) Revised effective ionic radii and systematic studies of interatomic distances in halides and chalcogenides. Acta Crystallogr A 32:751–767
19. Yang C, Jin L, Xie W, Cava RJ (2023) Stuffed rare-earth garnets. Inorg Chem 62:21364–21370
20. Li M, Zheng X, Xue Z, Ding D, Feng H (2025) Suppression of antisite defects and enhancement of scintillation properties in LuAG:Pr single crystals by fluorine codoping. J Lumin 288:121598
21. Yang X et al (2024) Crystal growth and enhanced magneto-optical properties of a terbium aluminum gallium garnet crystal for Faraday isolators. CrystEngComm 26:3311–3316
22. Dong J, Lu K (1991) Noncubic symmetry in garnet structures studied using extended x-ray-absorption fine-structure spectra. Phys Rev B 43:8808–8821
23. Brandle CD, Barns RL (1974) Crystal stoichiometry of Czochralski grown rare-earth gallium garnets. J Cryst Growth 26:169–170
24. Yang C et al (2023) Erbium-excess gallium garnets. Inorg Chem 62:13731–13737
25. Kikugawa N (2024) Recent progress of floating-zone techniques for bulk single-crystal growth. Crystals 14:552
26. Slimi S et al (2025) Growth, structure, spectroscopic, and laser properties of Ho-doped yttrium gallium garnet crystal. Opt Express 33:2529–2541
27. Liu Z, Nakamura H, Akai T (2024) situ TEM/STEM investigation of crystallization in $Y_3Al_5O_{12}$:Ce at high temperatures inside a transmission electron microscope. Small 20:2308001
28. Berry T, Ng N, McQueen TM (2024) Tools and tricks for single crystal growth. Chem Mater 36:4929–4944
29. Yoshikawa A et al (2013) Crystal growth and characterization of Ce:$Gd_3(Ga,Al)_5O_{12}$ single crystal using floating zone method in different O_2 partial pressure. Opt Mater 35:1882–1886
30. Zajíc F et al (2025) A fast GGAG:Ce(Mg) single crystal scintillator: LDFZM growth, characterization and electronic band structure calculation. Mater Adv 6:777–787
31. Kumar K et al (2022) Scalable and tunable Y_2O_3–MgO composite for infrared transparency applications. J Am Ceram Soc 105:3636–3646

32. Düvel A et al (2018) Tuning antisite defect density in perovskite-$BaLiF_3$ via cycling between ball milling and heating. J Phys Chem Lett 9:5121–5124
33. Gomez Alvarado SJ et al (2024) Advances in high-pressure laser floating zone growth: the Laser Optical Kristallmacher II (LOKII). Rev Sci Instrum 95:033903
34. Gomez Alvarado SJ et al (2025) High-pressure floating zone crystal growth of Sr_2IrO_4. Phys Rev Mater 9:053402
35. Serrano MD et al (2026) Tailoring Yb^{3+} energy levels by local configuration in the garnet structure: the case of $Ca_3(NbGa□)_5O_{12}$ laser single crystals as a model for Yb:YAG. J Mater Chem C 14:2902–2918
36. Xu S et al (2024) Thin-disk multi-pass amplifier for kilowatt-class ultrafast lasers. High Power Laser Sci Eng 12:e56
37. Zhang Q, Ueda J, Zheng R, Tanabe S (2024) Near-infrared thermometer based on Stark energy levels of Yb^{3+} in garnet. Phys Status Solidi A 221:2400302
38. Brown DC et al (2020) Yb:Lu_2O_3 hydrothermally grown single-crystal high-resolution absorption spectra obtained between 8 and 300 K. Appl Phys B 126:62
39. Topper B et al (2025) Yb:Lu_2O_3 single-crystal fiber: spectroscopy, amplification, and lasing. Opt Lett 50:2278–2281
40. Yang M et al (2025) Growth, spectral characteristics, and laser performance of Yb:$Lu_3Ga_5O_{12}$ crystals. J Alloys Compd 1010:178255
41. Nicolas J, Coutures J, Coutures JP, Boudot B (1984) Sm_2O_3–Ga_2O_3 and Gd_2O_3–Ga_2O_3 phase diagrams. J Solid State Chem 52:101–113
42. Makino H, Nakamura S, Matsumi K (1976) Lattice parameter variations in Czochralski grown gadolinium gallium garnet single crystals. Jpn J Appl Phys 15:415–419
43. Allibert M, Chatillon C, Mareschal J, Lissalde F (1974) Étude du diagramme de phase dans le système Gd_2O_3–Ga_2O_3. J Cryst Growth 23:289–294
44. Udalov YP, Rakhmankulov RM, Chemekova TY, Belousova OL (2003) Crystallization and phase equilibria in the Tb_2O_3–Ga_2O_3 system. Glass Phys Chem 29:200–201
45. Li BY et al (2024) Elucidating ultranarrow $^2F_{7/2}$ to $^2F_{5/2}$ absorption in ytterbium(□) complexes. Chem Sci 15:12451–12458
46. Álvarez-Pérez JO, Cano-Torres JM, Serrano MD, Cascales C, Zaldo C (2020) A probe of the radiation field magnetic component based on octahedral Yb^{3+} in the CaNbGa garnet–CNGG–single crystal. J Mater Chem C 8:7882–7889
47. Kalusniak S et al (2025) Growth, spectroscopy, and laser operation of Yb:$LaLuO_3$. Opt Mater Express 15:1924–1938
48. Guo R et al (2023) Exploration of the crystal growth and crystal-field effect of Yb^{3+} in orthorhombic $GdScO_3$ and $LaLuO_3$ crystals. Cryst Growth Des 23:3761–3768

49. Tan J et al (2026) Yb:YGG, crystal growth, concentration dependent, spectroscopy and the luminescence mechanisms. Infrared Phys Technol 156:106555
50. Álvarez-Pérez JO et al (2021) A roadmap for laser optimization of Yb:$Ca_3(NbGa)_5O_{12}$-CNGG-type single crystal garnets. J Mater Chem C 9:4628–4642
51. Zorenko Y et al (2004) Luminescence of excitons and antisite defects in the phosphors based on garnet compounds. Radiat Meas 38:677–680
52. Ronda C (2025) Luminescent garnets: a tutorial overview. Opt Mater 162:116879
53. Bartosiewicz K et al (2020) Effects of La doping on the crystal growth, phase stability and scintillation properties of $Lu_3Al_5O_{12}$ single crystals. Mater Sci Eng B 261:114677
54. Przybylińska H et al (2014) Rare-earth antisites in lutetium aluminum garnets: influence on lattice parameter and Ce^{3+} multicenter structure. Opt Mater 36:1515–1519
55. Bartosiewicz K et al (2024) Engineering atomic size mismatch in Pr^{3+}, La^{3+} codoped $Lu_3Al_5O_{12}$ garnet single crystals for tailored structure and functional properties. J Alloys Compd 985:174078
56. Legrand W et al (2026) Lattice-tunable substituted iron garnets for low-temperature magnonics. Adv Funct Mater 36:2503644
57. Squires AG, Scanlon DO, Morgan BJ (2020) Native defects and their doping response in the lithium solid electrolyte $Li_7La_3Zr_2O_{12}$. Chem Mater 32:1876–1886
58. Lei C, Qian Z, Ma Y, Ahuja R (2025) What is the role of a magnetic Mo antisite defect on carrier relaxation and spin dynamics in 2–D MoS2? Nano Lett 25:7378–7384
59. Fan K et al (2024) Vibrational and magnetic states of point defects in bilayer $MoSe_2$. J Am Chem Soc 146:33561–33568
60. Ding H et al (2026) Enhanced internal magnetic field for long-cycle NCM-Li all-solid-state batteries via dual-inhibition of anode dendrite and cathode cation disorder. Adv Mater 38:e73186

Figures

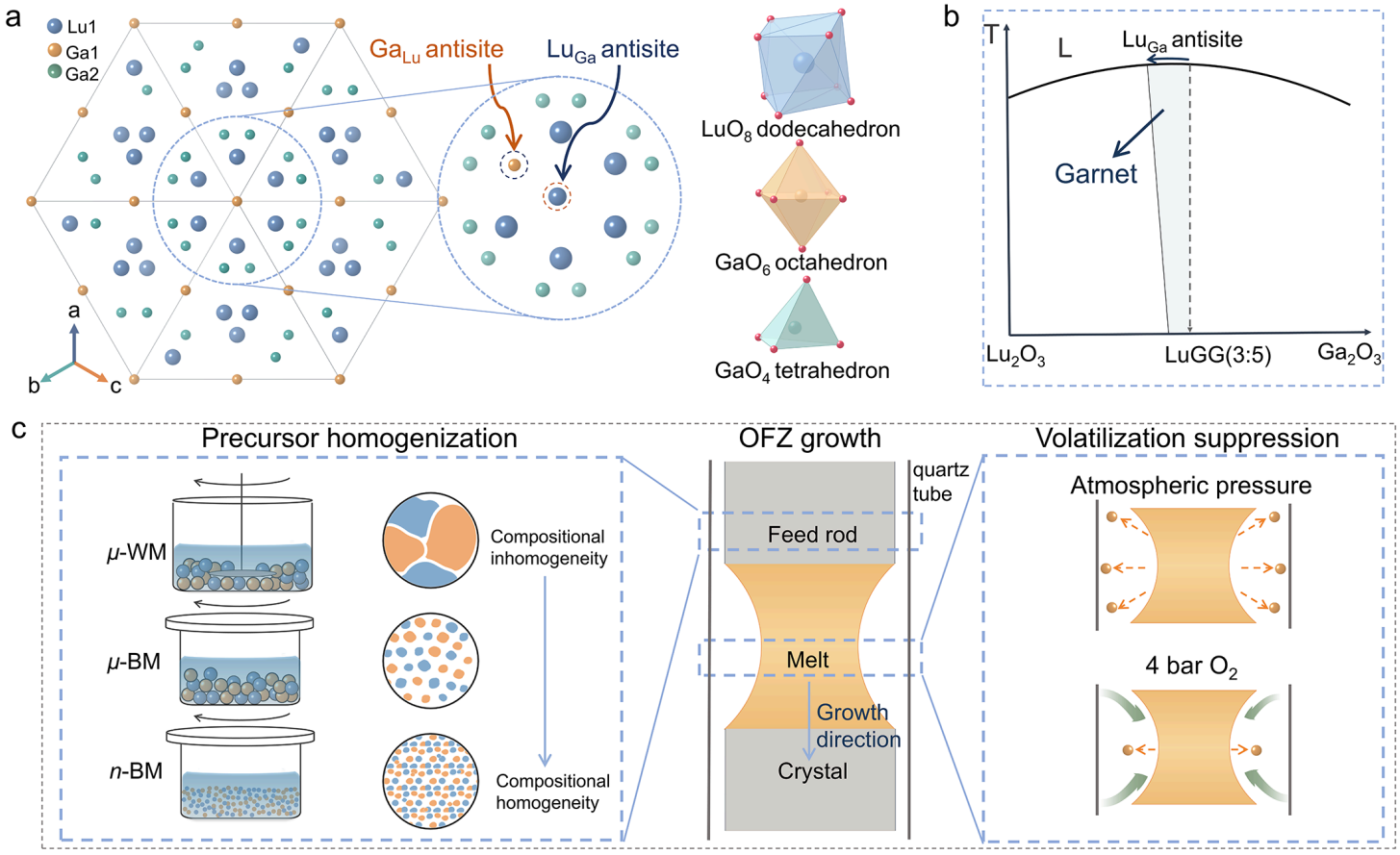


Figure 1

Antisite defect regulation strategy for LuGG crystals. (a) Schematic illustration of the LuGG crystal structure, showing cation polyhedra and the two possible antisite defect configurations (Lu_{Ga} and Ga_{Lu}). (b) Schematic Lu_2O_3-Ga_2O_3 phase diagram, demonstrating that the garnet phase preferentially stabilizes on the Lu-rich composition side, giving rise to an intrinsic propensity for Lu_{Ga} antisite defect formation. (c) Schematic of the antisite defect regulation approach for LuGG during OFZ crystal growth, implemented via precursor homogenization and suppression of Ga volatilization. *μ*-WM, *μ*-BM, and *n*-BM denote wet-mixed micron-sized powders, ball-milled micron-sized powders, and ball-milled nano-sized precursor powders, respectively.

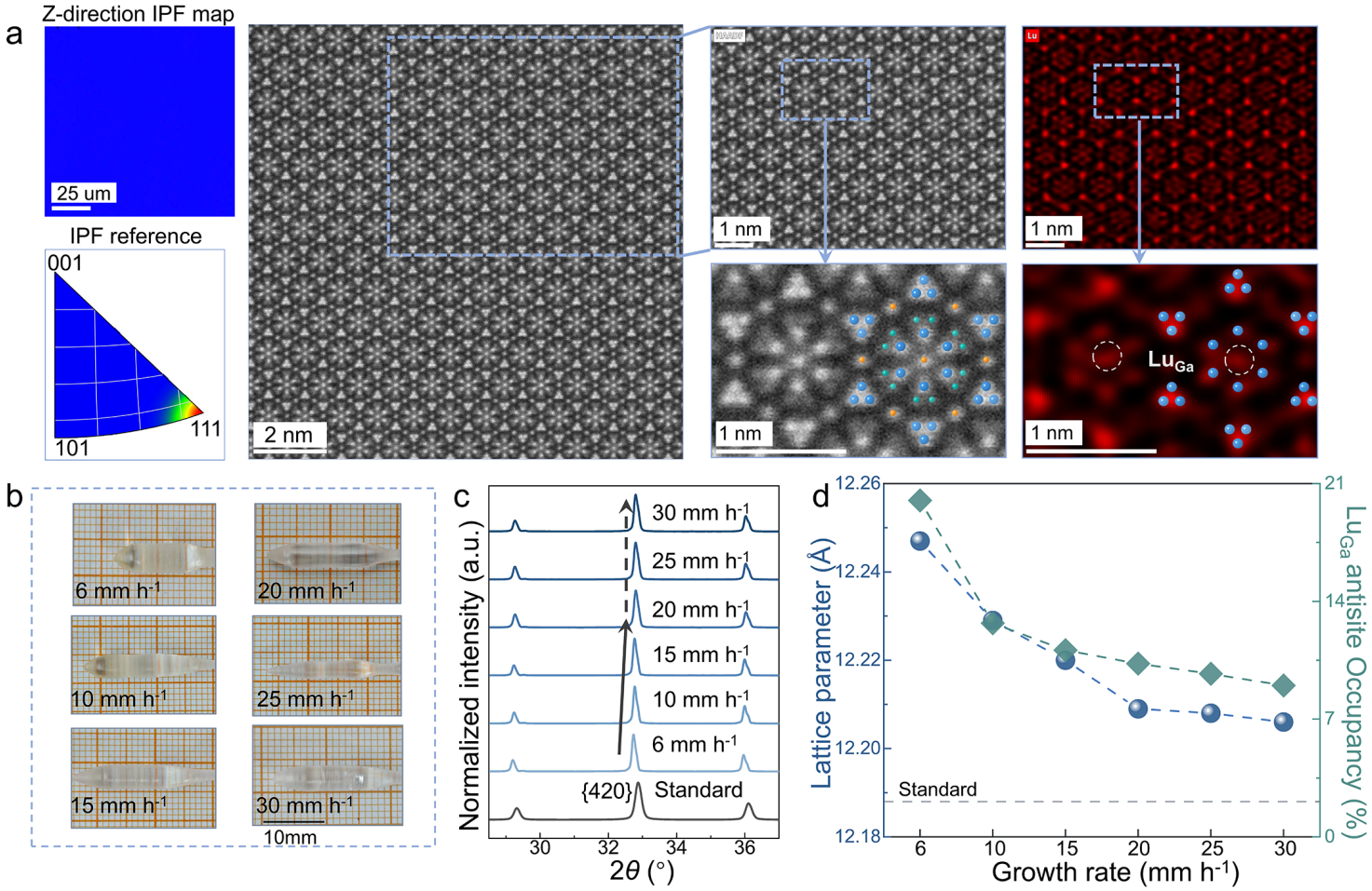


Figure 2

Growth-rate dependence of antisite defect formation in LuGG crystals prepared with the *μ*-WM precursor. (a) Multimodal microstructural characterization of the *μ*-WM-6 crystal via EBSD, HAADF-STEM, and Lu EDS mapping. Along the <111> orientation, dashed circles clearly mark Lu_{Ga} antisite defects localized at octahedral sites. (b) Photographs of as-grown LuGG crystals obtained at different growth rates ranging from 6 mm h^{-1} to 30 mm h^{-1}. (c) Corresponding XRD patterns for crystals grown at different growth rates. (d) Refined lattice parameter and Lu_{Ga} antisite occupancy plotted as a function of growth rate.

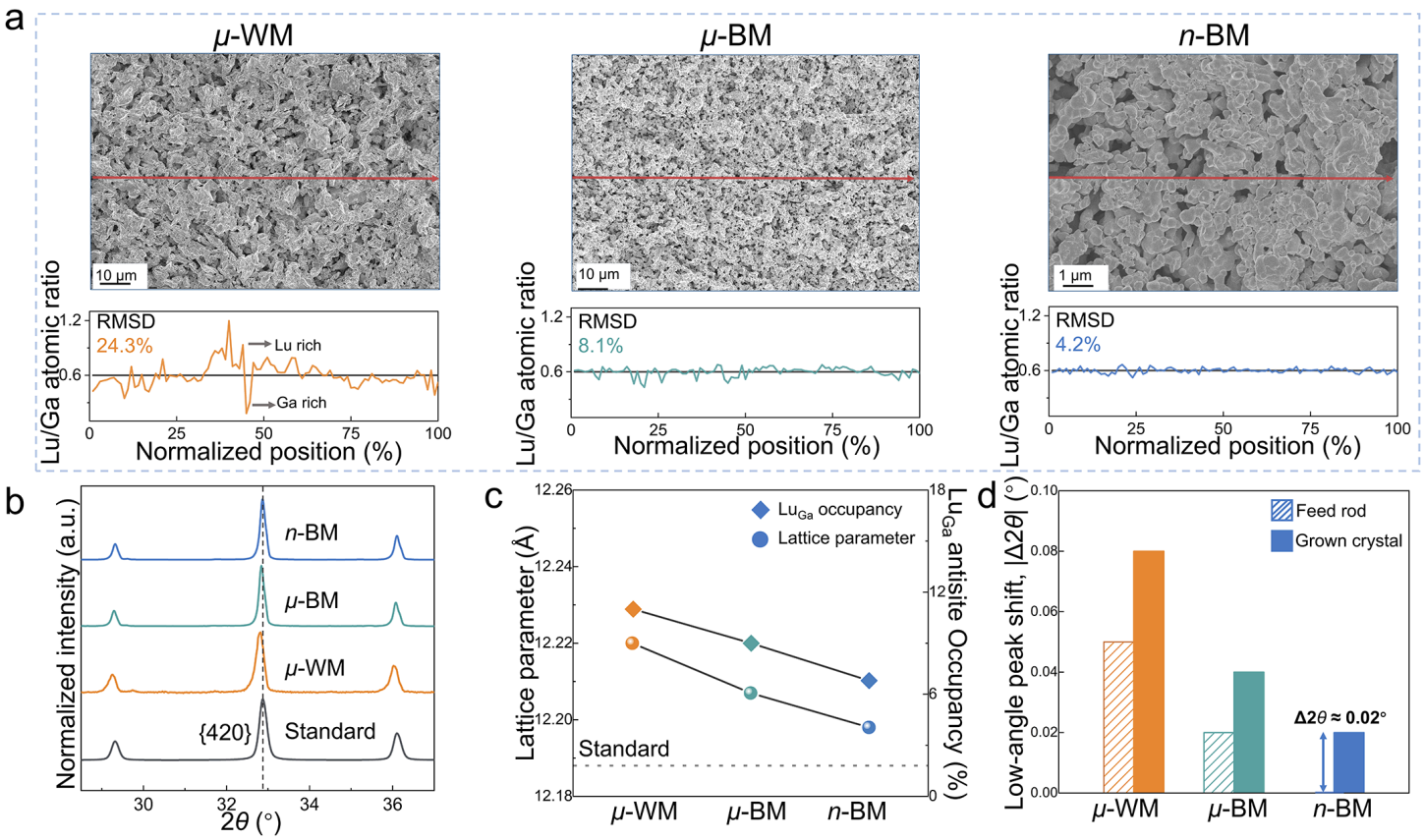


Figure 3

Effect of precursor homogenization on Lu_{Ga} antisite defect formation in LuGG crystals. (a) SEM images and corresponding Lu/Ga atomic ratio profiles of the *μ*-WM, *μ*-BM, and *n*-BM feed rods. (b) XRD patterns of the three different feed rods. (c) Lattice parameter and Lu_{Ga} antisite occupancy for crystals grown at atmospheric pressure, under a fixed growth rate of 15 mm h^{-1}. (d) Low-angle shift of the {420} XRD diffraction peak of feed rods and as-grown crystals, relative to the LuGG reference pattern.

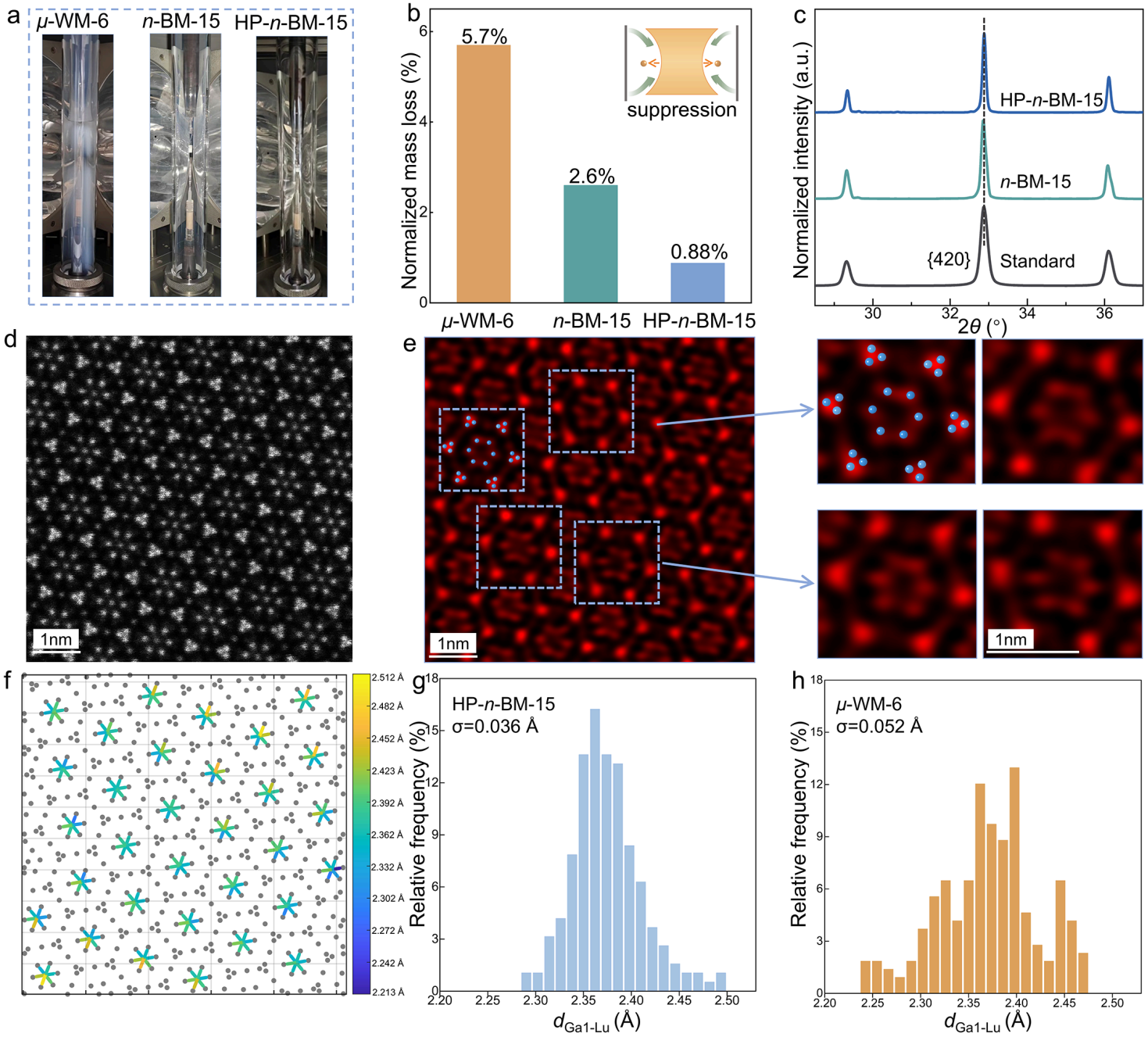


Figure 4

Antisite defect regulation and corresponding local structural analysis of LuGG via combined precursor homogenization and suppression of Ga volatilization. (a) Post-growth photographs of the growth system for *μ*-WM-6, *n*-BM-15, and HP-*n*-BM-15, showing distinct differences in Ga volatilization residue on the inner wall of the quartz tube. (b) Normalized mass loss during crystal growth. (c) Comparison of XRD patterns for *n*-BM-15 and HP-*n*-BM-15 crystal samples. (d,e) HAADF-STEM image and corresponding Lu EDS mapping of HP-*n*-BM-15 acquired along the <111> orientation, confirming that crystal growth under pressurized O_2 effectively suppresses Lu_{Ga} antisite defect formation. Scale bar, 1 nm for all four magnified images. (f) Mapping of projected d_{Ga1-Lu} distances between Ga1 sites and their

nearest-neighbor Lu sites. (g,h) Statistical comparison of the d_{Ga1-Lu} distance distribution between HP-*n*-BM-15 and *μ*-WM-6 crystals.

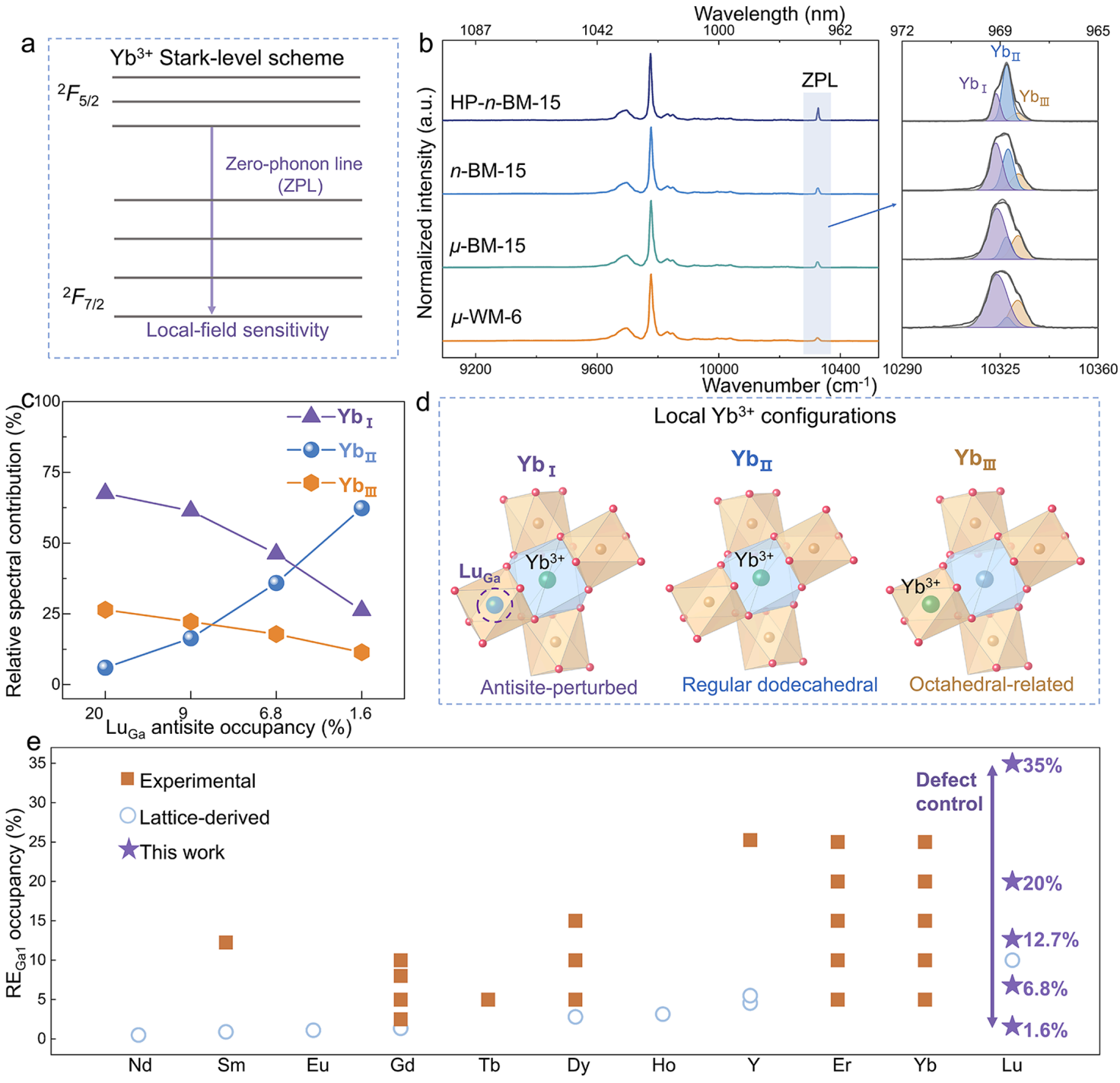


Figure 5

Antisite-modulated local crystal-field environments of Yb^{3+} in LuGG crystals. (a) Stark energy level scheme of Yb^{3+}, with the ZPL transition marked between the $^2F_{7/2}$ and $^2F_{5/2}$ multiplets. (b) Low-temperature (78 K) emission spectra of four Yb:LuGG samples acquired under 940 nm excitation. The right panel shows the magnified ZPL region, where three distinct Yb_I, Yb_{II}, and Yb_{III} centers are resolved

via Gaussian fitting. (c) Relative integrated contributions of the three Yb centers at the ZPL position plotted as a function of Lu_{Ga} antisite occupancy. (d) Schematic illustration of local configurations for Yb_{I}, Yb_{II}, and Yb_{III} centers, assigned respectively to antisite-perturbed dodecahedral, regular dodecahedral, and octahedral-associated Yb^{3+} centers. (e) Reported octahedral antisite defect regulation by lanthanide RE cations in gallium garnets, demonstrating the broad-range controllable antisite defect engineering for LuGG crystals achieved in this work[23,24,41-44].

Supplementary Files

This is a list of supplementary files associated with this preprint. Click to download.

- SupplementaryInformation.docx